COASTAL ENGINEERING JOURNAL
2018, VOL. 60, NO. 4, 449–465
https://doi.org/10.1080/21664250.2018.1529261

ORIGINAL RESEARCH PAPER

Decelerating bores in channels and estuaries

Youkai Li and Hubert Chanson

School of Civil Engineering, The University of Queensland, Brisbane, Australia

ABSTRACT

Decelerating bores are commonly seen in shorelines, estuaries and rivers in forms of swash run-up, tidal bores, tsunami bores. A decelerating bore propagating upstream can gradually change its shape, finally becoming an arrested bore, i.e. a stationary hydraulic jump. New experiments on decelerating bores against an adverse slope were conducted. Observations highlighted various types of arrested bores: fully breaking jumps, partially breaking jumps and non-breaking undular jumps. Measurements were repeated at least 25 times to obtain ensemble-averaged data with regards to instantaneous median and fluctuations of free-surface elevation, velocity components and turbulent shear stresses. An abrupt rise of free-surface elevation and immediate decrease in stream-wise velocity were observed during the passage of a decelerating bore. The arrival of decelerating bores induced some drastic increase of instantaneous free-surface fluctuations and all velocity components. Large-amplitude Reynolds stresses and extreme Reynolds stress fluctuations occurred in the same phase during and after the passage of decelerating bores. Histogram analysis of instantaneous normal and tangential Reynolds stresses suggested a preponderance of relatively smaller amplitudes. The upstream propagation of decelerating bores increased the probability density of large normal and tangential Reynolds stresses, yielding extrema vastly exceeding the critical threshold for inception of sediment motion.

ARTICLE HISTORY
Received 24 November 2017
Accepted 10 September 2018

KEYWORDS
Decelerating bores; tidal bores; physical modelling; free-surface measurements; reynolds stress; turbulence

1. Introduction

Tidal bores are basically compression waves of tidal origin, developing in estuaries where the bathymetry amplifies the tidal range, in presence of macro-tidal conditions with low fresh water levels (Tricker, 1965; Lighthill, 1978; Liggett, 1994; Chanson, 2011a). Figure 1 presents photographs of two typical tidal bores in natural streams: Qiantang River bore in China and Dordogne River bore in France. A bore is essentially a discontinuous hydrodynamic shock, sometimes called a traveling hydraulic jump (Henderson, 1966; Hornung, Willert, and Turner, 1995). The front of a bore is defined as the area between the location of the beginning of free-surface rise and the location of the first crest. A bore front, especially a breaking one, normally embraces some discontinuity of the pressure and velocity fields as well as intense turbulence (Lighthill, 1978; Hornung, Willert, and Turner, 1995). The unsteady turbulent mixing during the bore propagation is responsible for major sediment processes and upstream advection of suspended matters succeeding the leading front, as evidenced during field observations (Wolanski et al., 2004; Greb and Archer, 2007; Chanson, 2011a; Keevil, Chanson, and Reungoat, 2015; Furgerot et al., 2016; Reungoat, Leng, and Chanson, 2017) and laboratory measurements (Khezri and Chanson, 2012, 2015). The form of a bore front is characterized by its Froude number Fr_1, defined as:

$$Fr_1 = \frac{V_1 + U}{\sqrt{g \times \frac{A_1}{B_1}}} \tag{1}$$

where A_1, B_1 and V_1 are respectively the initial flow cross-section area, free-surface width and flow velocity (positive downstream) immediately prior to the bore arrival; U denotes the bore celerity (positive upstream) and g is the gravity acceleration (Chanson, 2012). For the case of a rectangular channel, the simplified definition of bore Froude number is $Fr_1 = (V_1 + U)/(g\times d_1)^{1/2}$, where d_1 denotes the initial flow depth immediately in front of the tidal bore. The Froude number of a tidal bore must exceed unity, i.e. $Fr_1 > 1$ (Henderson, 1966; Liggett, 1994). When a tidal bore has a Froude number between 1 and 1.2–1.3, it is an undular bore: the bore front is characterized by a smooth rise of the free-surface, followed by a train of strong secondary free-surface undulations (Treske, 1994; Koch and Chanson, 2008; Chanson, 2010a) (Figure 1(b)). If a tidal bore has a Froude number between 1.2–1.3 and 1.5–1.8, it is a weak breaking bore with secondary waves behind the bore front. A breaking bore occurs when its Froude number exceeds 1.5–1.8: the bore front is formed of an abrupt roller with intense air entrainment and highly

CONTACT Hubert Chanson h.chanson@uq.edu.au

(a)

(b)

Figure 1. Natural tidal bores observed in rivers. (a) Breaking tidal bore of Qiantang River at Yanguan (China) on September 18 2016 – Bore propagation from background to foreground, viewed from Qiantang River Bore Observation Station (QBOS). (b) Undular tidal bore of Dordogne River at St Pardon (France) on the afternoon of December 15 2016 – Bore propagation from left to right, viewed from left bank.

turbulent motion (Chanson, 2010b; Leng and Chanson, 2015a) (Figure 1(a)).

Although most laboratory studies were conducted in horizontal rectangular channels, a wide range of prototypical phenomena encompass bores that propagate upstream into channels of downward slope: e.g. tidal bores and hydraulic jumps (Chanson, 2011b), tsunami bores (Shuto, 1985; Yasuda, 2010; Adityawan et al., 2012; Tanaka, Yagisawa, and Yasuda, 2012). Related applications include rejection surges in canals of hydroelectric plants during sudden decrease in power output (Ponsy and Carbonnell, 1966), swash run-up against run-down on beach slopes (Kobayashi and Johnson, 2001). When a bore travels upstream against downstream-running flow on a slopping channel, the bore celerity decelerates progressively and can be expected to transform into a stationary hydraulic jump. On a mobile bed, the upstream propagation of a bore induces deformation of the bed, associated initially with the transformation into a quasi-stationary jump, before vanishing because of changes in mobile bed profile (Parker, 1996; Bellal *et al*., 2003). The entire process may also be associated with some cyclic behavior of bed form creation and destruction (Grant, 1997; Parker and Izumi, 2000). Related studies on stationary hydraulic jumps include (Carling, 1995; MacDonald et al., 2009).

In this paper, a systematic laboratory investigation was presented on the upstream propagation of decelerating bores and their transformation processes from traveling bores into stationary hydraulic jumps. New experiments were conducted in a relatively large flume with a fixed PVC bed. Detailed observations included photographing of bore shape characteristics, high-frequency free-surface sampling and flow velocity measurements for six different flow conditions. For each flow condition, the experiments were repeated more than 25 times to derive some ensemble-averaged results. Different types of arrested bores were observed at the end of upstream propagation of decelerating bores. Both ensemble-averaged and instantaneous fluctuations of free-surface, flow velocities and Reynolds shear stresses were analyzed and compared, emphasizing the highly turbulent processes along with decelerating bore passages. The object of current research is to characterize the seminal features of turbulent mixing with decelerating bore passages in channels and estuaries.

2. Physical modeling

2.1. Presentation

In experimental fluid dynamics, any physical modeling is expected to deliver accurate predictions of prototypical flow behaviors (Novák and Cabelka, 1981; Foss, Panton, and Yarin, 2007). A laboratory study should be based on the fundamentals of similitude, to guarantee the reliability of extrapolating modeling results to flows at full scale. The quantitative modeling results should be non-dimensionalised to ensure they are most extensively valid. Accordingly, dimensional analysis of selected non-dimensionalised parameters is the fundamental way to conduct the extrapolation of physical modeling results.

To apply dimensional analysis to any fluid dynamic conditions, the related dimensional parameters should encompass essential fluid properties, physical constants, geometrical size of flume and initial flow conditions (Liggett, 1994). For a bore traveling in a rectangular flume, the dimensional analysis treats the instantaneous turbulent flow properties at a spatial location (x, y, z) and at a time t as functions of the surge characteristics, initial flow conditions, flume geometrical dimensions and basic fluid properties:

$$\frac{d}{d_c}, \frac{V_i}{V_c}, \frac{P}{\rho \times g \times d_c}, \frac{\tau_{ij}}{\rho \times V_c^2}, \ldots = \mathrm{F}\left(\frac{x}{d_c}, \frac{y}{d_c}, \frac{z}{d_c}, t \times \sqrt{\frac{g}{d_c}}, \frac{V_1 + U}{\sqrt{g \times d_1}}, \rho \times \frac{(V_1 + U) \times d_1}{\mu}, \frac{W}{d_c}, S_o, \frac{k_s}{d_c}, \frac{g \times \mu^4}{\rho \times \sigma^3}, \ldots\right) \quad (2)$$

where d denotes the instantaneous flow depth, V_i denotes the i-component of the instantaneous velocity, P denotes the instantaneous pressure, τ_{ij} denotes the instantaneous Reynolds stress tensor component, i, j = x, y, z, x is the stream-wise coordinate, y is the horizontal transverse coordinate, z is the normal coordinate measured upwards perpendicular to the channel bed, d_c denotes the critical flow depth, V_c denotes the critical flow velocity, t denotes the time, U denotes the bore celerity, d_1 denotes the initial flow depth, V_1 denotes the initial flow velocity, S_o denotes the channel slope: $S_o = \sin\theta$ with θ denoting the angle between the bed and the horizontal, k_s denotes the equivalent roughness height of the channel bed, W denotes the channel width, ρ denotes the fluid density, μ denotes the fluid dynamic viscosity, and σ denotes the surface tension between air and water. In right-hand side of Equation (2), the fifth term is the bore Froude number Fr_1 and the sixth term is the Reynolds number Re, while the tenth term is the Morton number Mo determined by fluid properties and gravity constant only.

Conventional methods of hydraulic modeling are basically relied on geometrically similar models. In such approaches, the modeling fluid flow conditions can represent the prototypical flow conditions when they share similarity of form, similarity of motion and similarity of forces (Liggett, 1994; Chanson, 2004). In physical modeling, true similarity can only be ensured when each dimensionless parameter in model is strictly equal to the one in prototype. Scale effects might be inevitable if one or more dimensionless parameters are of different values between the laboratory study and full-scale application. Considering the tidal bore in the natural river (Figure 1), and the one in an experimental flume (Figure 2): how can we minimize the scale effects when extrapolating the physical modeling results to prototype?

Traditionally, open channel flows are analyzed using the Froude similarity (Henderson, 1966; Viollet et al., 2002; Chanson, 2004). Herein for a propagating bore, the Froude number is confirmed to be an significant dimensionless parameter based on momentum considerations (Lighthill, 1978) and it is also in accord with implicitly of basic theoretical analysis to select Froude similitude (Liggett, 1994; Chanson, 2012). However, viscous effects are not negligible in dominating turbulent shear flows. Surface tension, meanwhile, may be significant in breaking bores. A true kinematic and dynamic similarity of tidal bore flows can only be achieved when physical modeling and full-scale application share identical Froude, Reynolds and Morton numbers, which cannot be attained using geometrically similar models. Current research was only based on a Froude similitude as for most open channel hydraulic models, and therefore the critical flow depth d_c and critical flow velocity V_c were used respectively as characteristic length and velocity scales. Reynolds numbers of current experimental flows in the flume were estimated to be ~3 × 10^5. These flow conditions can be representative of a small full-scale manmade waterway.

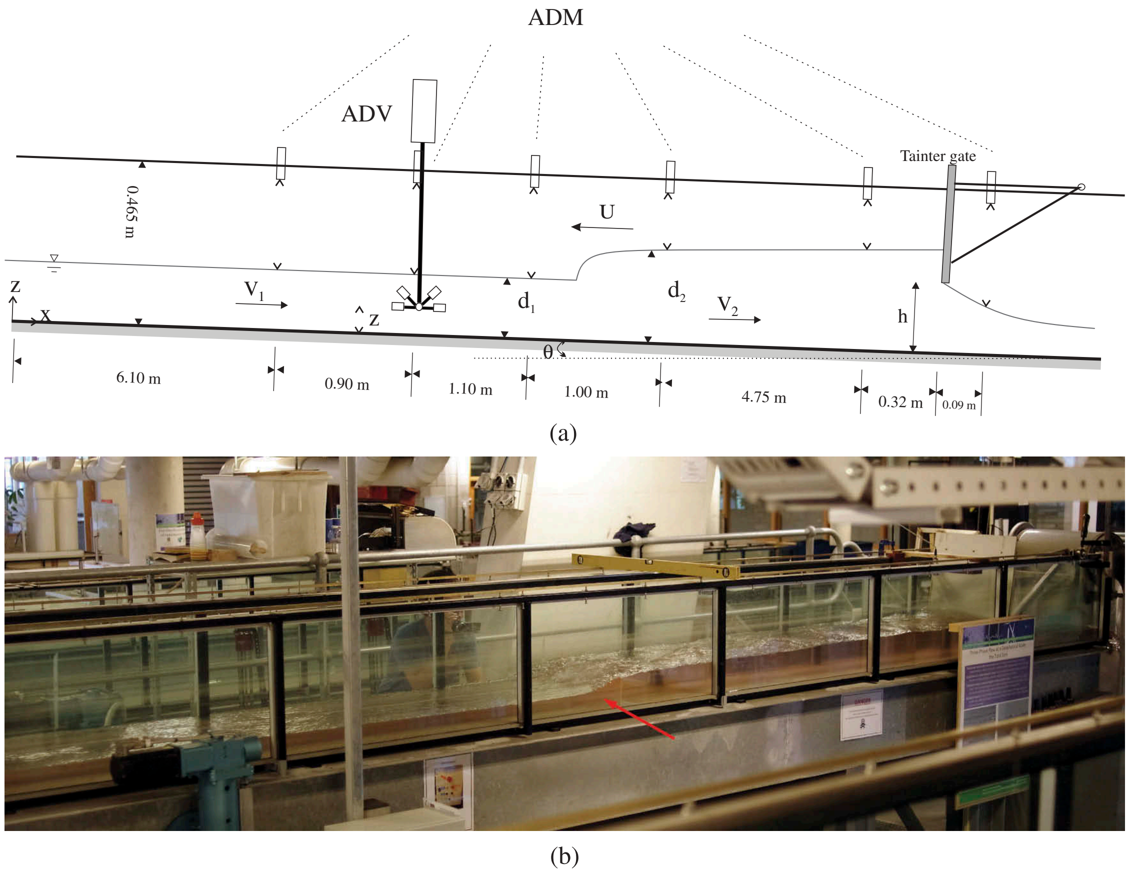

Figure 2. Experimental flume and definition sketch – Bore propagation from right to left. (a) Definition sketch. (b) Initial bore propagation at x = 11.5 m shortly after gate closure – Flow condition (Run 1): Q = 0.039 m^3/s, d_1, S_o = 0.0068, h = 0.080 m – Arrow pointing to toe tip.

2.2. Experimental facility and instrumentation

New experiments were carried out in a rectangular tilting channel with smooth PVC bed and glass sidewalls. The geometry of this facility is 15 m long, 0.5 m wide and 0.5 m high, previously used by Yeow, Chanson, and Wang (2016) (Figure 2). The water supply was provided by a constant head reservoir, feeding a wide upstream intake structure, passing through a set of flow straighteners and converging into the initially steady flow in the 15 m long measurement area. The test flow rates were measured by a Venturi flowmeter installed on the supply line with the error limited to 10^{-4} m^3/s. A Tainter gate was installed close to the downstream end of the channel at $x = x_{gate}$ = 14.17 m, where x is the longitudinal distance from the upstream end of the 15 m long test section.

Video recording was carried out using a DSLR camera Canon™ EOS 1200D (movie mode: 25 fps; resolution: 640 × 480 px), a camcorder Sony™ HDR-XR160 (movie mode: 25 fps, 1440 × 1080 px), and a DSLR camera Pentax™ K-3 (movie mode: 50 fps, 1920 × 1080 px). In steady flows, the flow depths were measured by a sharp pointer gauge, with the precision of ±0.5 mm. The unsteady flow depths were recorded by non-intrusive acoustic displacement meters (ADMs) Microsonic™ Mic+25/IU/TC. The ADMs were installed above the channel centreline at x = 14.26 m (immediately downstream of Tainter gate), 13.85 m (immediately upstream of Tainter gate), 9.10 m, 8.10 m, 7.00 m and 6.10 m. Before the unsteady flow measurements, all ADMs must be calibrated against the pointer gauge measurements in steady flows. The ADM sampling rate was 200 Hz and the data was collected by an acquisition system NI™ USB-6212 BNC driven by NI-DAQmx software.

The flow velocities were measured by a Nortek™ acoustic Doppler velocimeter (ADV) equipped with a side-looking fixed probe. The ADV control volume was placed at x = 7.00 m on the channel centreline. The nominal velocity range was set to ±2.5 m/s, with an accuracy of ±1% of measured value ±1 mm/s. The transmit length was selected as 0.3 mm with the sampling volume of 1.0 mm. The ADV sampling rate was also 200 Hz in accord with the ADMs. The vertical elevation of the ADV control volume was set by a fine adjustment system connected to a HAFCO™ M733 digimatic vertical scale unit. The vertical position of the ADV probe could be controlled within 0.025 mm and the longitudinal position had a precision of ±2 mm.

Table 1. Experimental setup and selected flow conditions.

Run	Q (m^3/s)	S_o	d_1[a] (m)	Fr_o[a]	U[a] m/s	Fr_1[a]	d_c (m)	V_c (m/s)	Remark
1	0.039	0.0110	0.059	1.76	0.037	1.79	0.086	0.917	Arrested bore.
2	0.039	0.0068	0.066	1.47	0.037	1.52	0.086	0.917	Arrested bore.
3	0.061	0.0110	0.085	1.59	0.039	1.62	0.116	1.065	Arrested bore.
4	0.061	0.0068	0.074	1.95	0.039	1.96	0.116	1.065	Arrested bore.
5	0.039	0	0.125	0.57	0.966	1.44	0.086	0.917	Horizontal channel.
6	0.061	0	0.162	0.60	0.927	1.34	0.116	1.065	Horizontal channel.

[a] flow properties recorded at x = 7 m.

2.3. Experimental flow conditions and bore generation

Two initially steady flow rates (Q = 0.039 m^3/s and 0.061 m^3/s) and three channel slopes (S_o = 0, 0.0068 and 0.0110) were used in current laboratory study, although the decelerating bore experiments were conducted for only two bed slopes: S_o = 0.0068 and 0.0110, where $S_o = \sin\theta$ and θ is the channel tilting angle from the horizontal. Experiments on the horizontal bed (S_o = 0) were performed to obtain a reference data set. During all the experiments, the initially steady flow presented a partially-developed vertical velocity profile for $0 < x < 9$ m, including at the ADV measurement location x = 7.00 m. Detailed velocity measurements in steady flows characterized that the stream-wise velocity distribution within the developing boundary layer presented a 1/8th power law in average, while the boundary layer growth followed:

$$\frac{\delta}{x} = \frac{28.7}{\mathrm{Re}_x^{0.52}} \tag{3}$$

where δ denotes the boundary layer thickness and Re_x denotes the Reynolds number defined as function of the longitudinal distance x and free-stream velocity V_{max}. Within the turbulent boundary layer on a flat surface, $\delta/x \propto 1/\mathrm{Re}_x^{0.20}$ (Chanson, 2014; Schlichting and Gersten, 2017). The present results showed a different growth rate, which reflected differences in inflow and boundary conditions, as well as an accelerating flow motion. For all flow conditions, the boundary shear stress in initially steady flow was calculated to be $\tau_o \approx 1.2$–1.8 Pa at x = 7.00 m, using the von Karman momentum integral equation (Liggett, 1994; Chanson, 2014).

For all experiments, the instrument sampling was triggered 1 min before the bore was generated, and the data acquisition was stopped once the bores became arrested. The Tainter gate was lowered down to a pre-set opening h slightly higher than the free-surface. An adjunctive gate was attached to the Tainter gate and used to generate bores: it was pushed down within 0.2 s, left partially closed for 3–4 s with an opening about 5 mm less than initial d_1 and lifted up in less than 0.2 s. Table 1 lists all the detailed setup for each selected flow condition. Herein the relatively steep channel slopes induced supercritical initial conditions with the initial flow Froude number Fr_o larger than unity, while the same flow rates only generated sub-critical initial flows in the same channel with S_o = 0. Besides, the decelerating bore celerity was much smaller than that in the horizontal channel (Table 1).

3. Basic flow patterns

3.1. Presentation

During the upstream propagation of decelerating bores on slopes, their basic flow patterns were documented by visual observation and camera recording. The bores were breaking ones immediately after generation for all the six investigations listed in Table 1. A breaking bore was typically formed of a short area of mild surface rise and a succeeding turbulent roller of intense air bubble entrainment (red arrow in Figure 2(b)). For a decelerating bore, during its upstream propagation in the slopping channel, the bore properties gradually evolved and especially the bore Froude number Fr_1 was reduced with further traveling distance. The similar trends were also observed in the experiments by Chanson (2011b). For comparison, in the same channel at horizontal (S_o = 0) with the same flow rate, the experiments did not present evident changes in bore properties through the whole channel, as shown by Run 5–6 of current experiments and also by Yeow, Chanson, and Wang (2016).

For a decelerating bore traveling upstream, its evolutionary shape was determined by the initial flow and new boundary conditions. For a specific flow condition (e.g. Run 4), the decelerating bore could be always fully breaking without shock waves at the front, even until it stopped at the final arrest location, i.e. a breaking hydraulic jump. For the other flow conditions, the arrested bore could be a partially breaking jump with two non-intersecting shock waves close to sidewalls and weak secondary waves behind bore front (Figure 3), or a smooth undular jump with a pair of shock waves intersecting at the centreline and a train of strong secondary waves following behind (Figure 4).

3.2. Bore propagation and celerity

The upstream propagation of each decelerating bore was tracked by moving video recording following the

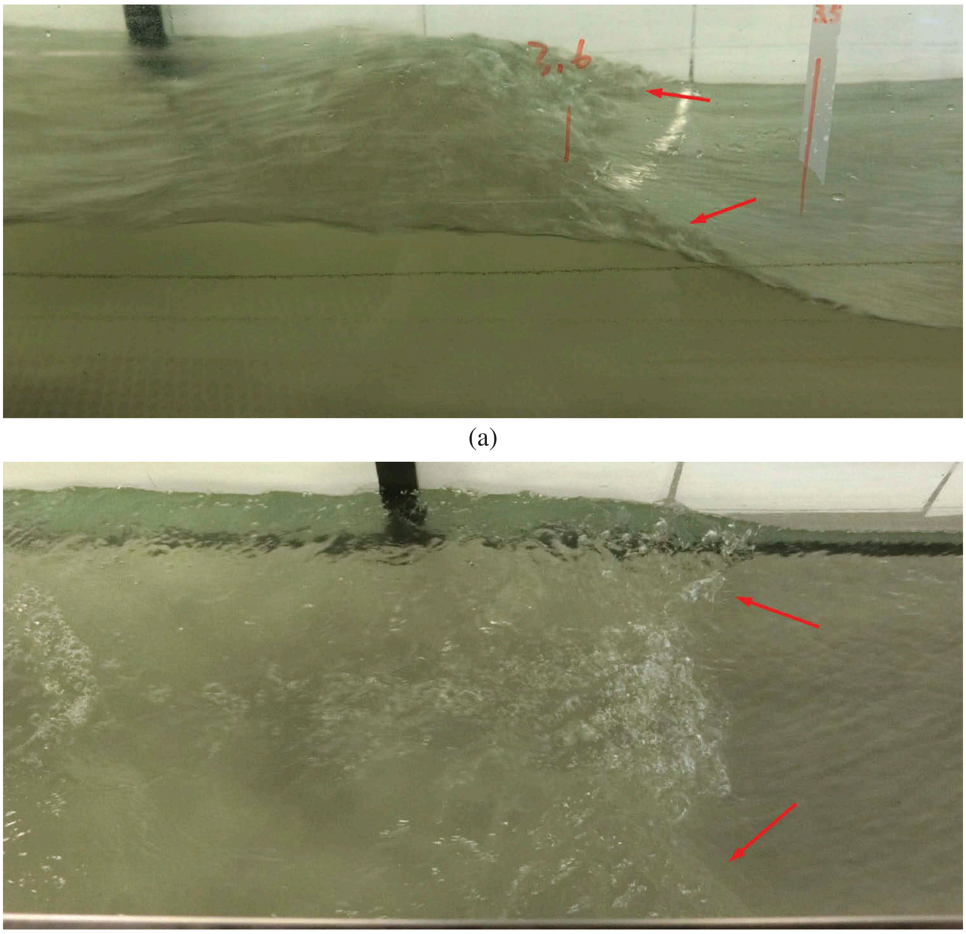

(a)

(b)

Figure 3. Photographs of an arrested breaking bore with two shock waves (red arrows) close to sidewalls and weak secondary waves behind bore front: (a) side view; (b) top view – Flow condition: $Q = 0.039$ m^3/s, $S_o = 0.0110$, $h = 0.065$ m, $Fr_1 = 1.5$ at $x = 3.5$ m (Run 1).

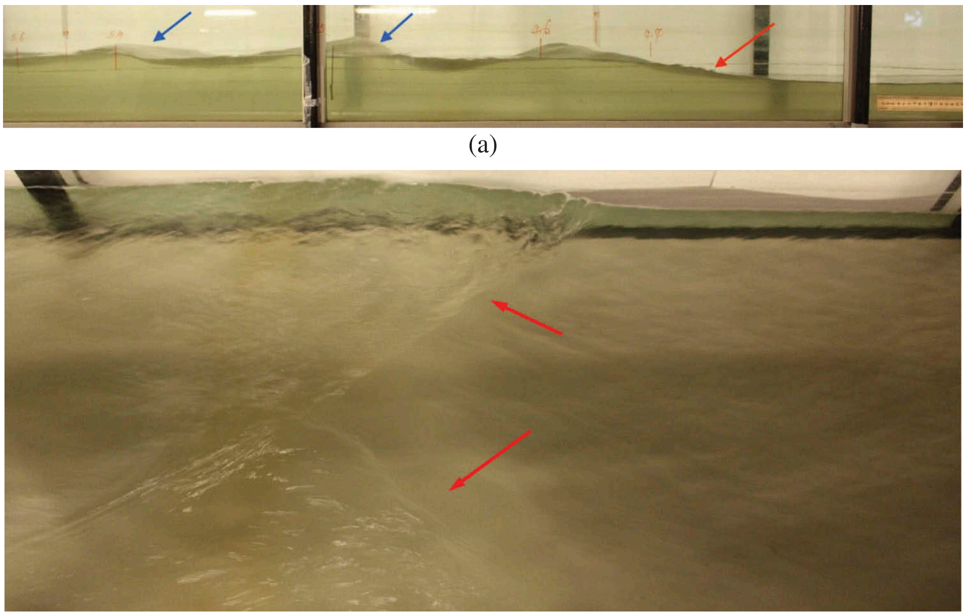

(a)

(b)

Figure 4. Photographs of an arrested non-breaking undular bore with a pair of shock waves (red arrows) intersecting at the centreline and a train of strong secondary waves (blue arrows) following behind: (a) side view; (b) top view – Flow condition (Run 2): $Q = 0.039$ m^3/s, $S_o = 0.0068$, $h = 0.080$ m, $Fr_1 = 1.3$ at $x = 4.3$ m.

bores through the sidewall. The position of a decelerating bore front was determined by targeting its toe tip (i.e. position of maximum free-surface curvature prior to the first crest) at different times (Figure 2(b)). Frame-by-frame analysis of the video yielded the bore arrival times at various locations along the channel, and hence the related celerities. Figure 5(a) illustrates the non-dimensionalised bore locations versus the dimensionless propagation distance since their generation: $(x_{gate}-x_s)/x_{gate}$, where x_{gate} = 14.17 m (location of Tainter gate), x_s denotes the bore front location and d_c denotes the critical depth of initially steady flow – $d_c = (Q^2/(g\times W^2))^{1/3}$ – with W the channel width (W = 0.495 m). Figure 5(b) presents the corresponding dimensionless bore celerity U/V_c data where V_c denotes the critical velocity of initially steady flow, i.e. $V_c = (g \times Q/W)^{1/3}$. Figure 5(c) shows details of the variations in bore celerity shortly after gate closure. For Runs 1 to 4 (Table 1), all the decelerating bores stopped propagating prior to reaching the upstream-end tank, which is demonstrated by the bold lines in Figures 5(a,b).

The generation of bores was realized by rapid gate closure as described previously in Section 2.3. A bore could form instantly following the gate being partially or fully shut down. The newly-generated bore immediately accelerated and gained the maximum celerity at a short distance from the gate. However, once the bore traveled further upstream, its celerity started to decrease (Figures 5(b,c)). The bore celerity rapidly reduced to 50% of the maximum value, due to the combined effects of steep bed slope, adjunctive gate removal and boundary friction. For each flow condition, the arrival times of decelerating bores became more scattered between different repeats at the locations farther away from the Tainter gate (Figure 5(a)). It took about 350–450 s for the decelerating bores to fully stop traveling upstream and transformed into stationary hydraulic jumps. By contrast, for the experiments of Run 5 and 6 (Table 1), the bores only spent less than 20 s traveling through the whole 15 m long horizontal test section. The transformation of a decelerating bores was a much slower process in comparison with the tidal bore propagation in a horizontal flumes, as indicated by Chanson (2011b) who recorded a decelerating bore spent 5–10 min transforming into a stationary hydraulic jumps. Based on the Froude similitude, the entire process should last longer at full scale in natural streams.

3.3. Discussion: final hydraulic jump features

The arrested bore was observed to shift about its longitudinal position with an "oscillation regime": it was not a truly stationary jump. Longitudinal oscillations of hydraulic jump toes has been recorded in previous studies, such as Long et al. (1991), Chanson and Gualtieri (2008), Murzyn and Chanson (2009) and Wang (2014). Long et al. (1991) indicated that the oscillating jump toes were associated with the

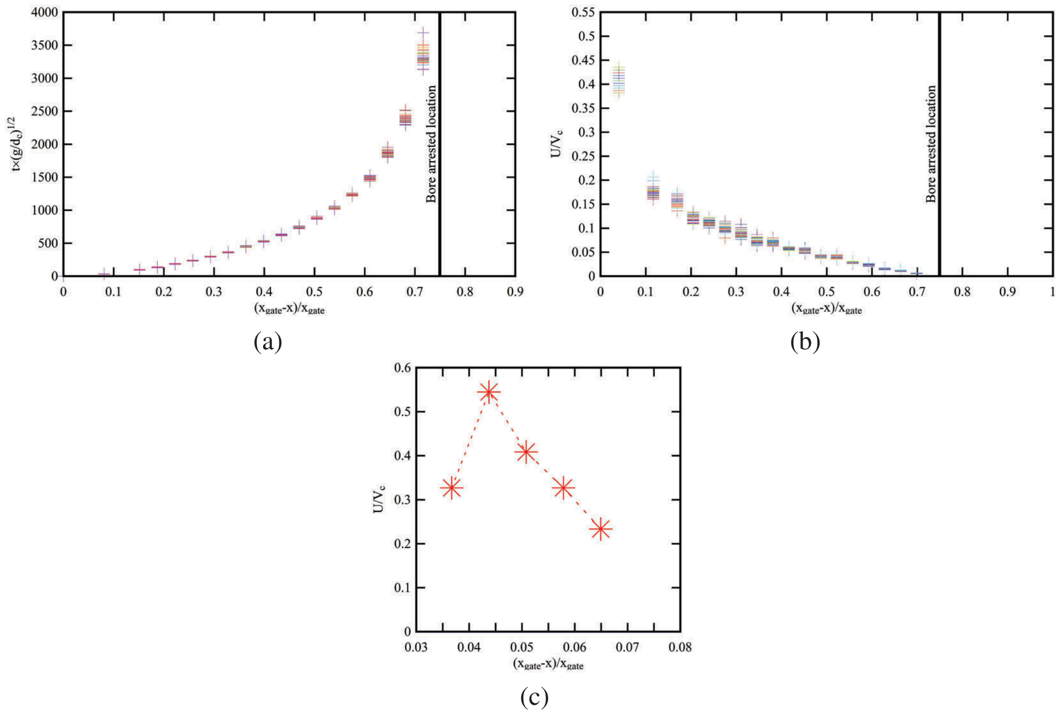

Figure 5. Characteristics of a decelerating bore propagating upstream (ensemble-average results) – Flow condition: Q = 0.039 m^3/s, S_o = 0.0110, h = 0.065 m, Fr_1 = 1.79 at x = 7.00 m (Run 1).

(a) Time variation of the bore front arrival at location x_s (b) Longitudinal variation of the bore celerity U (c) Longitudinal variation in bore celerity U immediately after gate closure turbulence structure development in rollers and the air entrapment at impingement area. For Runs 1 to 4 (Table 1), the final locations of the arrested bore were documented by video observations. Video recording started after the decelerating bores became fully stopped. Figure 6(a) presents a typical data set, showing based upon 2,200 frames post-processed, recorded 85 min after gate closure. In Figure 6(a), the data are presented in dimensional form as a function of time. The arrested bore front had a maximum location shift of about 0.08 m during the 90 s period. The autocorrelation functions (ACFs) of these time series are illustrated in Figure 6(b). Some oscillations at period of about 3 s were found for the arrested bore of Froude number $Fr_1 = 1.5$. For comparison, hydraulic jumps with Froude numbers of 3.0–7.2 had a jump toe longitudinal oscillation of 0.7–10 s (Wang, 2014). As pointed by Wang (2014), the oscillation regime might be linked to the air entrainment in central area of the arrested bore front, and this could possibly explain differences between experiments.

4. Ensemble-averaged observations

4.1. Free-surface properties

For a bore traveling upstream in a rectangular slopping flume, an analytical solution of the conjugate flow properties can be derived from considerations of mass and momentum conservation, yielding the ratio of conjugate depths as a function of the Froude number and channel slope (Chanson, 2012, 2013; Leng and Chanson, 2015a). It yields:

$$\frac{d_2}{d_1} = \frac{1}{2} \times \left(\sqrt{(1-\varepsilon)^2 + 8 \times \frac{Fr_1^{\ 2}}{1-\varepsilon}} - (1-\varepsilon) \right) \quad (4)$$

where d_1 is initial flow depth prior to bore arrival, d_2 is the conjugate flow depth behind bore front, and ε is a non-dimensionalised parameter defined as

$$\varepsilon = \frac{Vo \times S_o}{W \times d_1^{\ 2} \times (Fr_1^{\ 2} - 1)} \quad (5)$$

with W the channel width and Vo the volume of the control section encompassing the bore front.

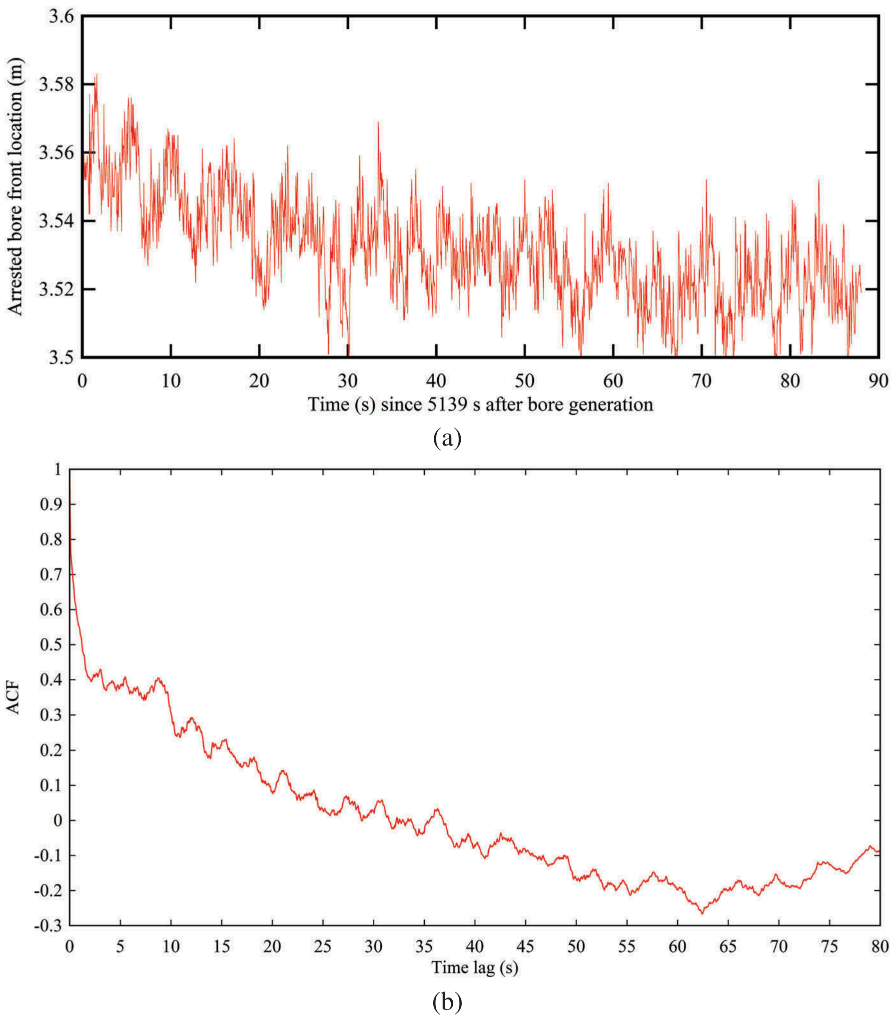

Figure 6. Time variations of the arrested bore: (a) Instantaneous location of arrested bore as a function of time; (b) Autocorrelation function of the instantaneous location of arrested bore – Flow condition (Run 1): Q = 0.039 m^3/s, S_o = 0.0110, h = 0.065 m, Fr_1 = 1.79 at x = 7.00 m and Fr_1 = 1.5 at x = 3.5 m.

Equation (4) shows that there is a positive correlation between the ratio of conjugate depths and the bed slope for the same Froude number. In the case of a bore in a smooth horizontal rectangular flume, Equation (4) can be reduced to the classic Bélanger equation: $d_2/d_1 = [(1 + 8\times \mathrm{Fr}_1^2)^{1/2}-1]/2$.

Due to the intense unsteadiness and turbulence in bore processes, a series of ensemble-average measurements were performed for all flow conditions to analyze the free-surface characteristics associated to the bore passages. For each listed flow condition in Table 1, the experiments were repeated more than 25 times to ensure the data reliability as discussed by (Leng and Chanson, 2015b). The median free-surface elevation d_{50} and the difference between third and first quartiles (d_{75}-d_{25}) were derived from the experimental data. The difference between third and first quartiles (d_{75}-d_{25}) characterized the instantaneous free-surface fluctuations. Some typical ensemble-averaged results are illustrated in Figure 7(a) with the time t = 0 indicating bore generation.

Through the ADM measurement section downstream x = 6.10 m, the decelerating bores always remain breaking ones during upstream propagation. An abrupt rise of free-surface was seen with the arrival of the roller. Following the bore front, some undulations of free-surface (secondary waves) occurred and the water depth gradually increased due to the backwater effect induced by the partially-closed Tainter gate. For the decelerating bores on the smaller slope (S_o = 0.0068), the secondary waves development with time was more evident though secondary waves were also seen on larger slopes. For either small slopes or large ones, the secondary wave periods became longer with time at each ADM sampling position. The bore passages also induced large free-surface fluctuations (d_{75}–d_{25}), which reached peak values immediately succeeding the breaking roller toe Figure 7(a).

The ratio of conjugate depths was estimated at several locations for all decelerating bores. The results are compared to Equation (4) in Figure 7(b). Current results are also compared with the theoretical considerations of Bélanger equation (S_o = 0) and the results from previous physical modeling in a smooth horizontal channel by Leng and Chanson (2017). As shown in (Figure 7(b)), all the datasets indicate a monotonic increase in conjugate depth ratio with increasing Froude number. Since $S_o \ll 1$ in the current experiments, the slope effect was not evident even though it did decelerate the bore propagation. For a constant water discharge, a larger bed slope tended to induce both larger bore Froude number and larger conjugate depth ratio d_2/d_1 within the experimental flow conditions.

4.2. Unsteady turbulent properties

The velocity measurements by the ADV during bore processes were all performed at x = 7.00 m. The collected dataset encompassed the stream-wise velocity V_x parallel to the bed slope positive downstream, transverse velocity V_y positive towards left sidewall and vertical velocity V_z normal to the channel bed positive upwards. Figure 8 illustrates typical ensemble-average results of Run 2 with the median water depth d_{50}, median velocity components V_{50} and instantaneous velocity fluctuations (V_{75}-V_{25}). For all the flow conditions, the decelerating bore front remained breaking at the central area and the bore Froude number Fr_1 was larger than 1.5 (x = 7.00 m). The passage of bore front induced a marked deceleration around 50% to the longitudinal velocity V_x (Figure 8(a)). The vertical velocity V_z presented some slight perturbation associated with the bore front passage, however much weaker than the decrease of stream-wise velocity V_x (Figure 8(c)). The bore celerity U was estimated to be 0.02 – 0.04 m/s at ADM

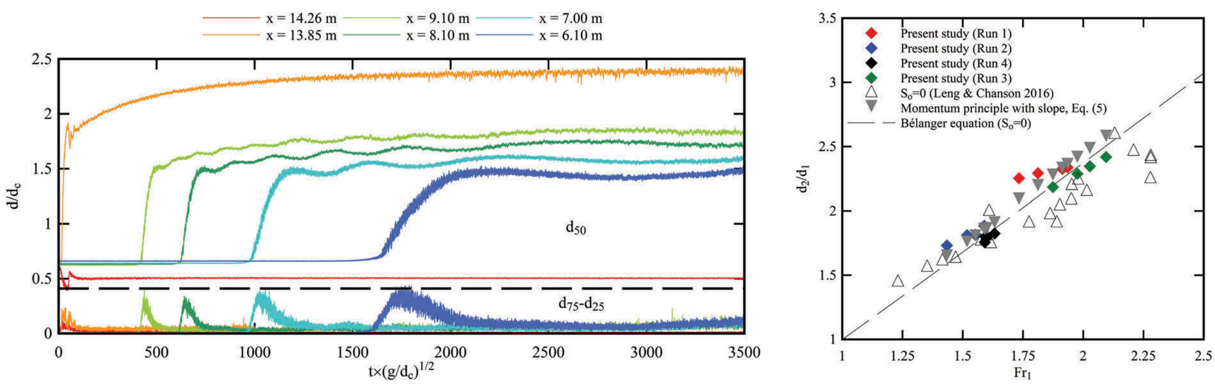

(a) (b)

Figure 7. Ensemble-averaged free-surface properties during the upstream propagation of decelerating bores. (a) Time-variations of ensemble-averaged median free-surface elevations d_{50} and free-surface fluctuations (d_{75}-d_{25}) at different longitudinal locations – Flow condition (Run 3), Q = 0.061 m^3/s, S_o = 0.0110, h = 0.100 m, Fr_1 = 1.96 at x = 7.00 m.. (b) Conjugate depth ratio d_2/d_1 as a function of local bore Froude number Fr_1 – Comparison with horizontal slope data (Leng and Chanson, 2016), the momentum principle Equation (5) and the Bélanger equation.

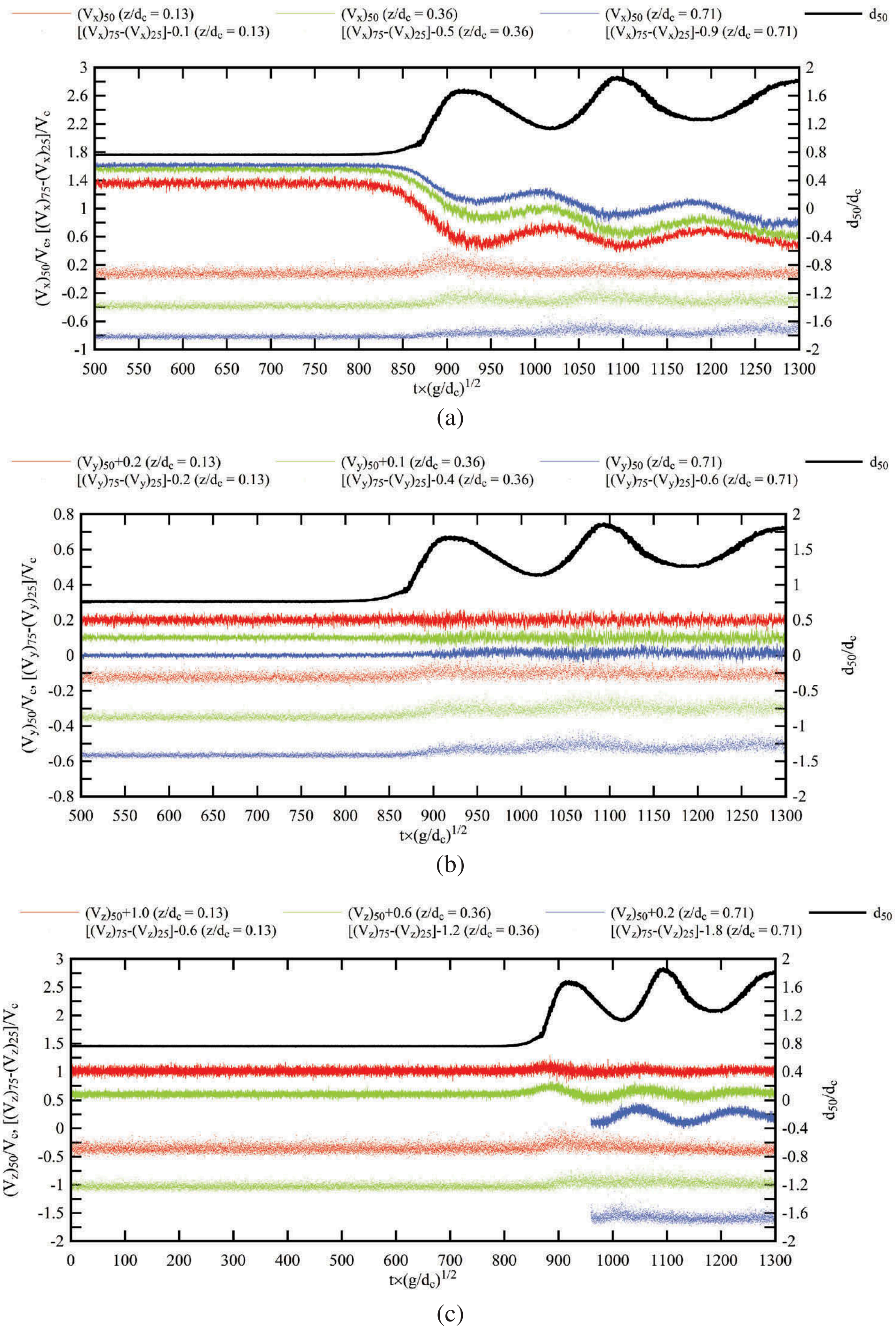

Figure 8. Time variations of ensemble-averaged median longitudinal, transverse and vertical velocity components (coloured lines) and velocity fluctuations (V_{75}-V_{25}) (coloured dots) at different vertical elevations z for decelerating bores locally synchronized at x = 7.00 m – Comparison with median water depth – Flow condition (Run 2): Q = 0.039 m^3/s, S_o = 0.0068, h = 0.080 m, Fr_1 = 1.52 at x = 7.00 m.

(a) Longitudinal velocity component V_x (b) Transverse velocity component V_y (c) Vertical velocity component V_z

sampling location, which was much slower than that of breaking bores in horizontal flumes of the experiments by Koch and Chanson (2009) and (Leng and Chanson, 2016). Therefore, the relative deceleration rate of V_x in current experiments was also much slower Furthermore, V_x always remained positive during the whole decelerating bore processes. Streamwise velocity reversal did not show up in current experiments, contrarily to measurements on a horizontal channel by Koch and Chanson (2009). This finding was basically in accord with the instantaneous velocity observations by Chanson (2011b) in decelerating bores.

For all the flow conditions, the transverse velocity V_y and vertical velocity V_z presented a mean value of zero, prior to the arrival of decelerating bores at x = 7.00 m (Figures 8(b,c)). At all vertical elevations, the longitudinal flow velocity component V_x experienced an abrupt decrease within the bore front passages. Meanwhile, the vertical flow velocity V_z

indicated some initial increase with passage of bore front and then some decrease afterwards, linked to the streamline curvature in association with the bore roller. All the ensemble-averaged velocity components V_x, V_y and V_z presented some oscillations responding to the streamline curvature induced by the secondary waves, as shown in Figure 8 for the decelerating bores of relative small Froude number $Fr_1 = 1.52$. These features were comparable to earlier undular bore experiments in a horizontal channel (Koch and Chanson, 2008; Leng and Chanson, 2016) as well as stationary undular hydraulic jump experiments (Chanson and Montes, 1995; Lennon and Hill, 2006).

The turbulent velocity fluctuations reached the peak values immediately following the bore front, for all the three velocity components (Figure 8). The maximum velocity fluctuations at a vertical elevation near the bed took place in advance of that at elevations closer to the water surface. The larger velocity fluctuations were also further observed closer to the bottom. Similar features were also exhibited in the tidal bore experiments in a horizontal flume by Leng and Chanson (2016). However, these features were different from those of stationary hydraulic jump experiments (Liu, Rajaratnam, and Zhu, 2004; Chachereau and Chanson, 2011), in which the stream-wise velocity fluctuations increased with further distance from the bottom for $z/d_1 < 1$.

4.3. Reynolds stress properties

The Reynolds stress tensor component is defined as $\tau_{ij} = \rho \times v_i \times v_j$, where ρ denotes the fluid density and v denotes the turbulent velocity fluctuation with subscript i, j = x, y, z (Piquet, 1999). It represents a shear stress on an area d$x\times$dy, d$y\times$dz or d$z\times$dx of an elementary control volume d$x\times$d$y\times$dz. For turbulent flows with rapid time variations, the instantaneous velocity V is typically decomposed into an average component V_{50} and a turbulent fluctuation v, i.e. $V = V_{50} + v$, where V_{50} is the ensemble average from sufficient repetitions of the same experiment (Bradshaw, 1971; Chanson and Docherty, 2012; Leng and Chanson, 2016). Therefore in current research, the normal Reynolds stresses $v_x\times v_x$, $v_y\times v_y$, $v_z\times v_z$ and tangential Reynolds stresses $v_x\times v_y$, $v_y\times v_z$, $v_z\times v_x$ were derived from the ensemble-averaged velocity measurements. Figure 9 presents typical results in terms of the median Reynolds stresses $(v_i\times v_j)_{50}$, third quartile of the normal stresses $(v_i\times v_i)_{75}$ and difference between third and first quartiles of the tangential stresses $(v_i\times v_j)_{75}$-$(v_i\times v_j)_{25}$ along with the median free-surface elevations d_{50} during decelerating bore processes, in which the velocity data were acquired at the vertical elevation of the initial flow mid-depth. The third quartile can characterize the representative large values while the quartile difference represents a characteristic fluctuation (Leng and Chanson, 2016). The time variations of median Reynolds stresses, third quartile of normal stresses and quartile difference of tangential stresses were all in the same phase (Figure 9). Their amplitudes all experienced significant increase with the passages of bore fronts and then reached the local extrema shortly after the roller toe. For most flow conditions, the global maxima were incurred by the bore fronts and then experienced overall decreasing trends with bores propagating further upstream, i.e. the first peak was the global maximum value (Figure 9(a)). However, for the Reynolds stresses and their fluctuations associated with decelerating bores of smaller Froude number (i.e. more undular), extrema larger than the first peak could occur with the secondary waves: the extreme Reynolds stresses and their fluctuations affected by growing secondary waves could be of comparable amplitudes, especially when the decelerating bores were not fully breaking (Figure 9(b)).

During the bore propagation, turbulence is generated by the extremely unsteady bore roller, by the bottom boundary friction, the coupling between free-surface deformations and pressure/velocity fluctuations, as well as the interactions between these different processes. Typical results of dimensionless median Reynolds stresses ($v_x\times v_x$, $v_z\times v_z$ and $v_z\times v_x$) are presented in Figure 10, showing the vertical structure at three different vertical elevations: near-bottom, middle-layer and near-surface referring to initial water level. Even though some vertical velocity data were not available at vertical elevations near the free-surface, the dataset gave a number of key features. Prior to the bore font arrival, the Reynolds stresses had larger values closer to the bottom, since bed friction was the dominant mechanism of turbulence generation. During the bore front passage, all the Reynolds stresses experienced peak values, with extreme values near the channel bottom. Behind the bore front, the Reynolds stresses increased substantially at the mid-layer and near-surface elevations compared to the initially steady flow data. In contrast, the near-bottom data had an opposite trend. Based on the above-mentioned features of Reynolds stress distribution, the turbulence intensity had a decreasing trend from bottom to surface in the supercritical steady flow, while it had a more homogenous vertical structure with relatively stronger amplitudes upper from the bottom in the bore-disturbed flow field. The passage of the bore modified totally the vertical turbulence structure. In the subcritical flow behind the bore, the bore front is apparently a stronger source of turbulence compared to the boundary layer.

The probability density functions (PDFs) of instantaneous Reynolds stresses were derived before, during and after the passages of decelerating bores. A

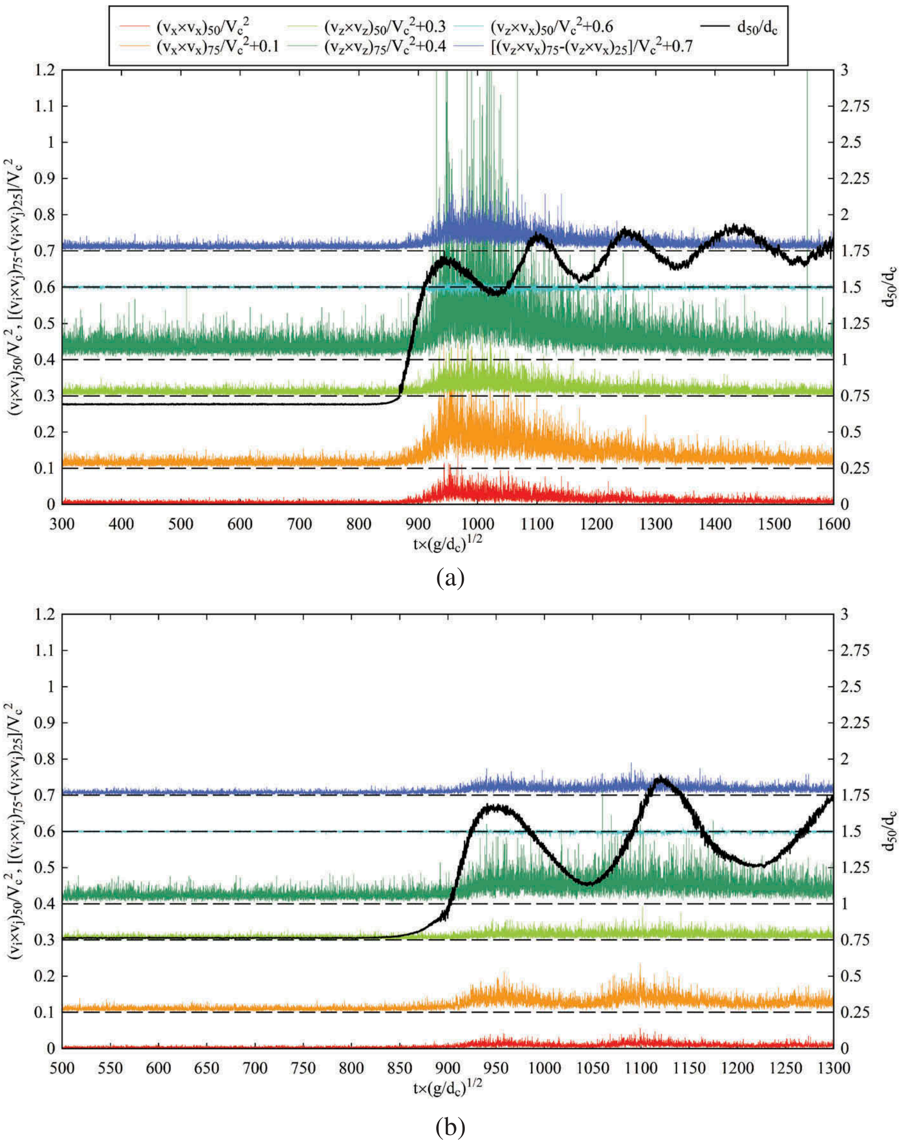

Figure 9. Time variations of Reynolds stresses and their fluctuations, referring to the median free-surface elevations from the ensemble-averaged results of decelerating bore experiments – Same legend for both figures; Curves separated by adding a constant as indicated in legends. (a) Run 1, Flow condition: $Q = 0.039$ m^3/s, $S_o = 0.0110$, $h = 0.065$ m, $Fr_1 = 1.79$ at x = 7.00 m, $z/d_c = 0.36$. (b) Run 2, Flow condition: $Q = 0.039$ m^3/s, $S_o = 0.0068$, $h = 0.080$ m, $Fr_1 = 1.52$ at $x = 7.00$ m, $z/d_c = 0.36$.

time span Δt is selected starting from immediate free-surface rise with bore arrival and ending at the maximum height of the first crest, which characterized the "during" bore front passage. Then the "before" and "after" periods were respectively Δt prior to the immediate free-surface rise and Δt following the peak of first crest. Typical data set of normal Reynolds stress tensor $v_x \times v_x$ and tangential Reynolds stress tensor $v_z \times v_x$ are presented in Figure 11 in dimensional form with class intervals of 0.0001 m^2/s^2. Since the celerity of a decelerating bore was relatively slow on the adverse slope, the selected time span was more than 30 s encompassing around 170,000 samples of instantaneous Reynolds stresses tensors for the ensemble-average experiment (Run 4, Table 1).

For all the decelerating bores in the tilted channel (Runs 1 to 4) and the tidal bores in the horizontal channel (Runs 5 and 6), all the normal and tangential Reynolds stress tensors were skewed toward 0 indicating a preponderance of relatively smaller amplitudes. The similar PDF patterns were also found in the experiments by Leng and Chanson (2016) as well as in the field measurements by Reungoat, Chanson, and Keevil (2015). During current experiments, at probability of 0.1‰ in the histograms, both the corresponding $v_x \times v_x$ and $v_z \times v_x$ bounded with the values exceeding 0.1 m^2/s^2. That is, the normal and tangential Reynolds stress tensors had the extrema larger than 100 Pa, assuming water density $\rho \sim 1000$ kg/m^3. Comparing the three selected time spans, the proportion of larger normal and tangential Reynolds stresses significantly increased in the order of "before," "during" and "after." The time span following the bore crest [Red symbols in Fig. (10)] included the distinct maximum number of larger Reynolds stresses. Therefore, the bore passage incurred

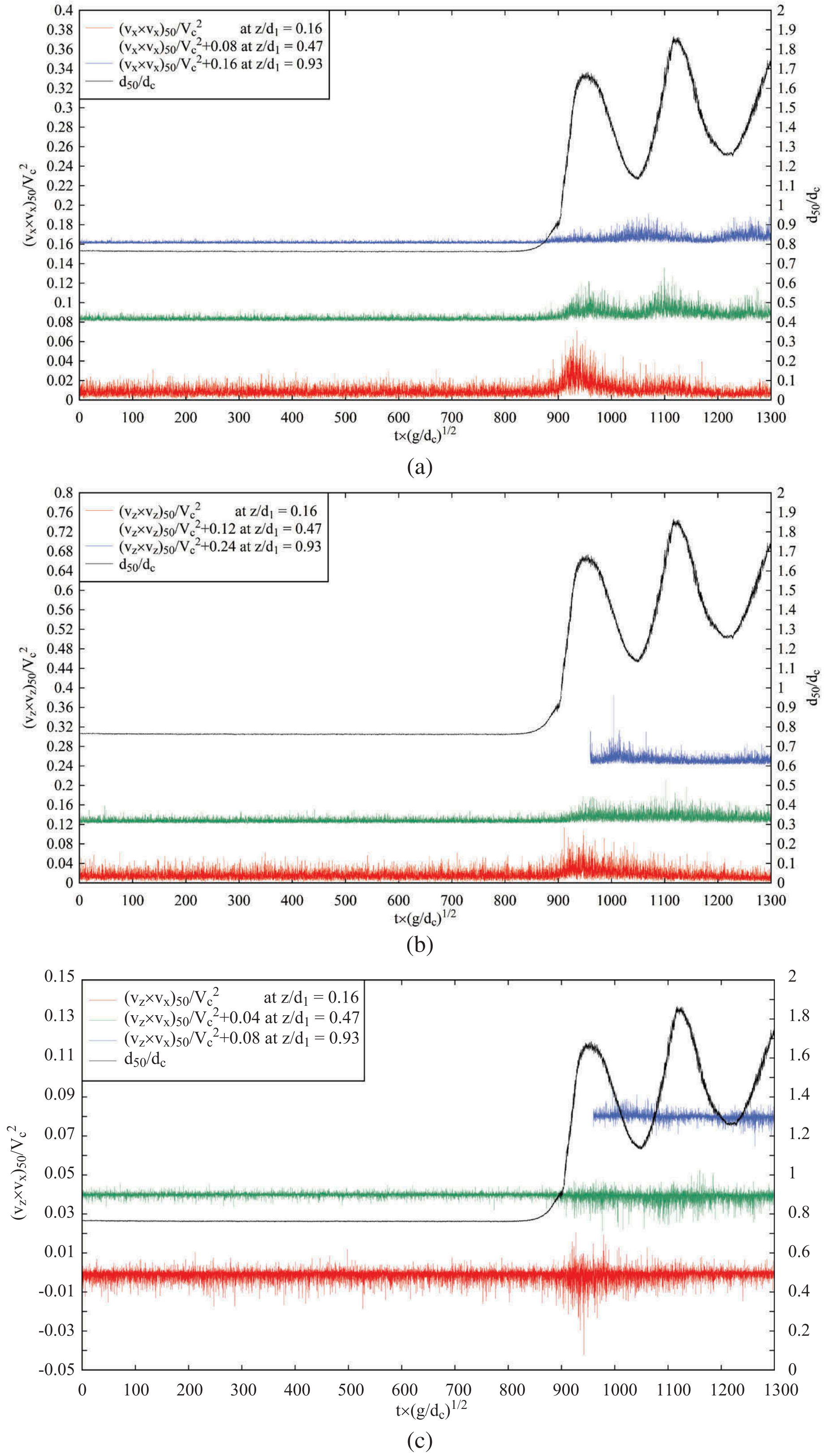

Figure 10. Time variations of dimensionless Reynolds stresses at different vertical elevations from the ensemble-averaged results – Flow conditions (Run 2): Q = 0.039 m^3/s, S_o = 0.0068, h = 0.080 m, Fr_1 = 1.52 at x = 7.00 m – Bore front arrival time: $t\times(g/d_c)^{1/2}$ = 892.

(a) Normal Reynolds stress tensors $v_x \times v_x$ (b) Normal Reynolds stress tensors $v_z \times v_z$ (c) Tangential Reynolds tensors $v_z \times v_x$

more large Reynolds stresses and the flow became more turbulent with the bore front passage. Similar to Leng and Chanson (2016), the extreme instantaneous Reynolds stresses induced by bore passage had one or two larger orders of the critical threshold for sediment motion in natural rivers and channels. It is more possible that sediment transportation and bed erosion can occur immediately after the bore front passage.

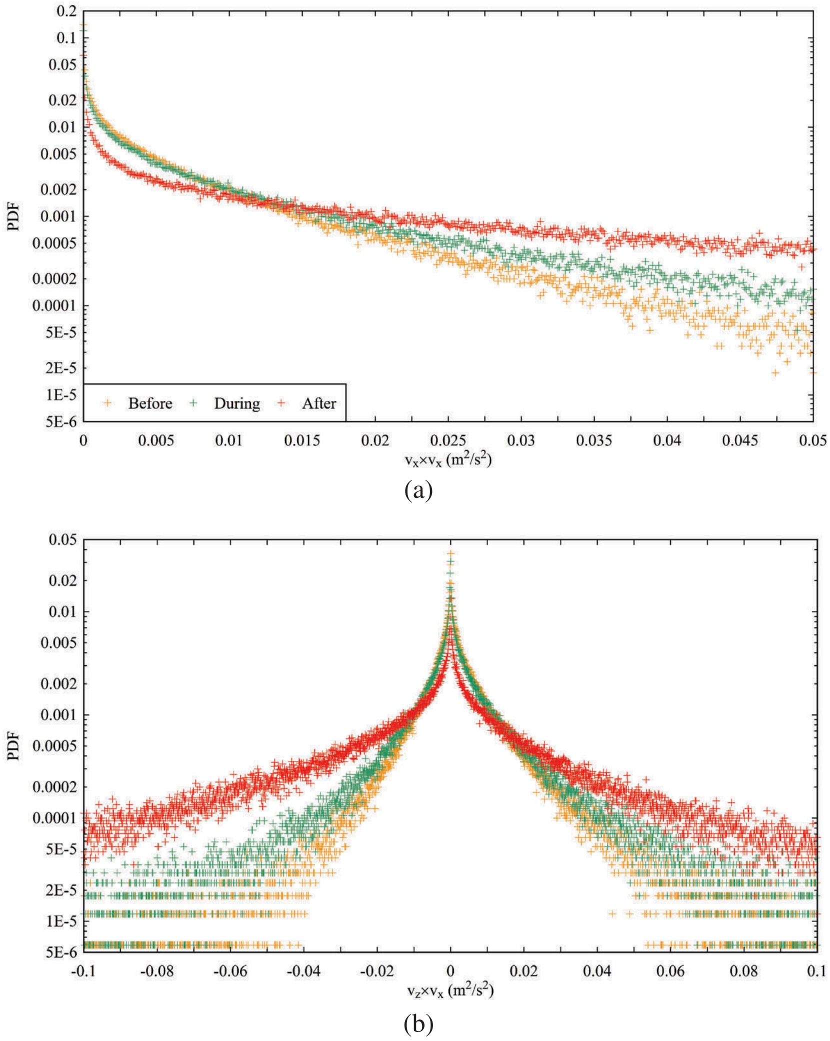

Figure 11. Probability density functions of turbulent Reynolds stress tensor before, during and after a decelaerating bore front passage – Flow conditions (Run 3): Q = 0.061 m^3/s, S_o = 0.0110, h = 0.100 m, Fr_1 = 1.96 at x = 7.00 m, z/d_1 = 0.54 – Same legend for both figures.

(a) Normal Reynolds stress tensors $v_x \times v_x$ (b) Tangential Reynolds tensors $v_z \times v_x$

5. Conclusion

Decelerating bores are commonly seen in natural estuaries and rivers as well in man-made waterways, e.g. swash run-up on beaches, tsunami bores in estuarine zones, tidal bores in rivers, rejection surges in hydropower canals, etc. Herein new experiments of decelerating bores on an adverse slope were conducted, focusing on the instantaneous and ensemble-averaged measurements of free-surface and velocity, as well as video tracking of decelerating bores transforming into stationary hydraulic jumps. For each flow condition, the experiments were repeated at least 25 times, performing an ensemble-averaged analysis to derive the instantaneous median and fluctuations of free-surface elevation, velocities and turbulent Reynolds stresses. The transformation of decelerating bores was also compared to the propagation of tidal bores in a horizontal channel.

The experiments featured the transformation of decelerating bores into stationary hydraulic jumps as a slow and complicated process. The entire process took one to two orders of magnitude longer compared to tidal bores traveling through the same channel on a horizontal slope. Visual observations indicated that the decelerating bore gradually changed its shape while celerity very-gradually decreased to zero. Video tracking highlighted the different forms of arrested bores: a fully breaking jump, a partially breaking jump with a pair of non-intersecting shock waves and some weak secondary waves, and a smooth undular jump with a pair of intersecting shock waves and a train of strong secondary waves, determined by the initial and boundary conditions. In practice, the arrested bore was not fully stationary: it shifted along the longitudinal direction with a non-consistent period.

An abrupt rise in free-surface and a decrease in stream-wise flow velocity were observed during the passage of a decelerating bore. The instantaneous free-surface and flow velocity fluctuations were significantly larger shortly after the decelerating bore arrival. Large amplitudes of Reynolds stresses and large Reynolds stress fluctuations occurred during the same phase, following the decelerating bore front. For decelerating bores of smaller Froude number, the maximum Reynolds stress amplitudes and fluctuations could be associated with strong secondary waves at the back of the first crest. The histogram of instantaneous normal and tangential Reynolds stresses indicated a preponderance of relatively smaller amplitudes with the passage of decelerating bores. Yet the upstream propagation of decelerating bores drastically increased the probability density of larger normal and tangential Reynolds stresses with extrema larger than 100 Pa, which vastly exceeded the critical threshold for sediment motion. In estuaries and rivers, the highly turbulent process of a decelerating bore may play a vital role in sediment transportation and bed erosion.

Acknowledgments

The authors thank Dr Hang Wang and Dr Xinqian Leng (The University of Queensland) for their valuable advice and comments. They acknowledge the technical assistance of Mr Jason Van Der Gevel and Mr Stewart Matthews (The University of Queensland). The financial support through the Australian Research Council (Grant DP120100481) is acknowledged.

Disclosure statement

No potential conflict of interest is reported by the authors.

Funding

This work was supported by the Australian Research Council [DP120100481].

ORCID

Youkai Li http://orcid.org/0000-0002-4281-5457
Hubert Chanson http://orcid.org/0000-0002-2016-9650

References

Adityawan, M. B., M. Roh, H. Tanaka, A. Mano, and K. Udo. 2012. ""Investigation of Tsunami Propagation Characteristics in River and on Land Induced by the Great East Japan Earthquake 2011." *Journal of Earthquake Tsunami* 6 (03): 1250033. doi:10.1142/S1793431112500339.

Bellal, M., B. Spinewine, C. Savary, and Y. Zech. 2003. "Morphological Evolution of Steep-Sloped River Beds in the Presence of a Hydraulic Jump: Experimental Study." In *Proc. 30th IAHR Congr., Int. Assoc. Hydraul. Res*, edited by J. Ganoulis and P. Prinos, 133–140. (Thessaloniki, Greece).

Bradshaw, P. 1971. *An Introduction to Turbulence and Its Measurement*, 218. Oxford, UK: Pergamon Press.

Carling, P. A. 1995. ""Flow-Separation Berms Downstream of a Hydraulic Jump in a Bedrock Channel,"." *Geomorphology* 11 (3): 245–253. doi:10.1016/0169-555X(94)00052-S.

Chachereau, Y., and H. Chanson. 2011. ""Free-Surface Fluctuations and Turbulence in Hydraulic Jumps,"." *Experimental Thermal Fluid Sciences* 35 (6): 896–909. doi:10.1016/j.expthermflusci.2011.01.009.

Chanson, H. 2004. *The Hydraulics of Open Channel Flow: An Introduction*, 630. 2nd Edition ed. Oxford, UK: Butterworth-Heinemann.

Chanson, H. 2010a. ""Undular Tidal Bores: Basic Theory and Free-Surface Characteristics,"." *Journal Hydraul Enggineering ASCE* 136 (11): 940–944. doi:10.1061/(ASCE)HY.1943-7900.0000264.

Chanson, H. 2010b. ""Unsteady Turbulence in Tidal Bores: Effects of Bed Roughness," J. Waterway, Port, Coastal, and Ocean Eng." *ASCE* 136 (5): 247–256. doi:10.1061/(ASCE)WW.1943-5460.0000048.

Chanson, H. 2011a. *Tidal Bores, Aegir, Eagre, Mascaret, Pororoca: Theory and Observations*, 220. Singapore: World Scientific.

Chanson, H. 2011b. ""Turbulent Shear Stresses in Hydraulic Jumps, Bores and Decelerating Surges,"." *Earth Surf Processing Landf* 36 (2): 180–189. doi:10.1002/esp.2031.

Chanson, H. 2012. ""Momentum Considerations in Hydraulic Jumps and Bores,"." *Journal of Irrigation and Drainage Engineering ASCE* 138 (4): 382–385. doi:10.1061/(ASCE)IR.1943-4774.0000409.

Chanson, H. 2013. ""Tidal Bore Research: Field Works, Physical Modeling, CFD & More,"." In *Proc. 35th IAHR Congr., Int. Assoc. Hydraul. Res*, 8–13, edited by W. Zhaoyin, J. Hun-wi Lee, G. Jizhang and C. Shuyou, Chengdu, China: IAHR.

Chanson, H. 2014. *Applied Hydrodynamics: An Introduction*. Leiden, The Netherlands: (CRC Press, Taylor & Francis Group. 448. 21 video movies.

Chanson, H., and N. J. Docherty. 2012. ""Turbulent Velocity Measurements in Open Channel Bores,"." *European Journal Mechanisms B Fluids* 32: 52–58. doi:10.1016/j.euromechflu.2011.10.001.

Chanson, H., and C. Gualtieri. 2008. ""Similitude and Scale Effects of Air Entrainment in Hydraulic Jumps,"." *Journal Hydraul Researcher IAHR* 46 (1): 35–44. doi:10.1080/00221686.2008.9521841.

Chanson, H., and J. S. Montes. 1995. ""Characteristics of Undular Hydraulic Jumps: Experimental Apparatus and Flow Patterns,"." *Journal Hydraul Engineering ASCE* 121 (2): 129–144. doi:10.1061/(ASCE)0733-9429(1995)121:2(129).

Foss, J., R. Panton, and A. Yarin. 2007. ""Nondimensional Representation of the Boundary-Value Problem,"." In *Handbook of Experimental Fluid Mechanics*, edited by C. Tropea, A. Yarin, and J. Foss, 33–83. Berlin, Heidelberg: Springer. doi:10.1007/978-3-540-30299-5_2.

Furgerot, L., D. Mouazé, B. Tessier, L. Perez, S. Haquin, P. Weill, and A. Crave. 2016. ""Sediment Transport Induced by Tidal Bores. An Estimation from Suspended Matter Measurements in the Sée River (Mont-Saint-Michel Bay, Northwestern France),"." *C. R. Geosci* 348 (6): 432–441. doi:10.1016/j.crte.2015.09.004.

Grant, G. E. 1997. ""Critical Flow Constrains Flow Hydraulics in Mobile-Bed Streams: A New Hypothesis,"." *Water Resources Researcher* 33 (2): 349–358. doi:10.1029/96WR03134.

Greb, S. F., and A. W. Archer. 2007. ""Soft-Sediment Deformation Produced by Tides in a Meizoseismic Area, Turnagain Arm, Alaska,"." *Geology* 35 (5): 435–438. doi:10.1130/G23209A.1.

Henderson, F. M. 1966. *Open Channel Flow*, 522. USA: MacMillan Company, New York.

Hornung, H. G., C. Willert, and S. Turner. 1995. ""The Flow Field Downstream of a Hydraulic Jump,"." *Journal Fluid Mechanisms* 287: 299–316. doi:10.1017/S0022112095000966.

Keevil, C. E., H. Chanson, and D. Reungoat. 2015. ""Fluid Flow and Sediment Entrainment in the Garonne River Bore and Tidal Bore Collision,"." *Earth Surf Processing Landf* 40 (12): 1574–1586. doi:10.1002/esp.3735.

Khezri, N., and H. Chanson. 2012. ""Undular and Breaking Tidal Bores on Fixed and Movable Gravel Beds,"." *Journal Hydraul Researcher IAHR* 50 (4): 353–363. doi:10.1080/00221686.2012.686200.

Khezri, N., and H. Chanson. 2015. ""Turbulent Velocity, Sediment Motion and Particle Trajectories under Breaking Tidal Bores: Simultaneous Physical Measurements,"." *Environment Fluid Mechanisms* 15 (3): 633–650. doi:10.1007/s10652-014-9358-z.

Kobayashi, N., and B. D. Johnson. 2001. ""Sand Suspension, Storage, Advection, and Settling in Surf and Swash Zones,"." *Journal Geophysics Reserach: Oceans* 106 (C5): 9363–9376. doi:10.1029/2000JC000557.

Koch, C., and H. Chanson. 2008. ""Turbulent Mixing beneath an Undular Bore Front,"." *Journal Coast Researcher* 24 (4): 999–1007. doi:10.2112/06-0688.1.

Koch, C., and H. Chanson. 2009. ""Turbulence Measurements in Positive Surges and Bores,"." *Journal Hydraul Researcher IAHR* 47 (1): 29–40. doi:10.3826/jhr.2009.2954.

Leng, X., and H. Chanson. 2015a. ""Breaking Bore: Physical Observations of Roller Characteristics,"." *Mechanisms Researcher Communicable* 65: 24–29. doi:10.1016/j.mechrescom.2015.02.008.

Leng, X., and H. Chanson. 2015b. ""Unsteady Turbulence in Expansion Waves in Rivers and Estuaries: An Experimental Study,"." *Environment Fluid Mechanisms* 15 (5): 905–922. doi:10.1007/s10652-014-9385-9.

Leng, X., and H. Chanson. 2016. ""Coupling between Free-Surface Fluctuations, Velocity Fluctuations and Turbulent Reynolds Stresses during the Upstream Propagation of Positive Surges, Bores and Compression Waves,"." *Environment Fluid Mechanisms* 16 (4): 695–719. doi:10.1007/s10652-015-9438-8.

Leng, X., and H. Chanson. 2017. ""Upstream Propagation of Surges and Bores: Free-Surface Observations." *Coast Engineering Journal* 59 (1): 1750003. doi:10.1142/S0578563417500036.

Lennon, J. M., and D. Hill. 2006. ""Particle Image Velocity Measurements of Undular and Hydraulic Jumps,"." *Journal Hydraul Engineering ASCE* 132 (12): 1283–1294. doi:10.1061/(ASCE)0733-9429(2006)132:12(1283).

Liggett, J. A. 1994. *Fluid Mechanics*, 495. New York, USA: McGraw-Hill.

Lighthill, J. 1978. *Waves in Fluids*, 504. Cambridge, UK: Cambridge University Press.

Liu, M., N. Rajaratnam, and D. Z. Zhu. 2004. ""Turbulence Structure of Hydraulic Jumps of Low Froude Numbers,"." *Journal Hydraul Engineering ASCE* 130 (6): 511–520. doi:10.1061/(ASCE)0733-9429(2004)130:6(511).

Long, D., N. Rajaratnam, P. M. Steffler, and P. R. Smy. 1991. ""Structure of Flow in Hydraulic Jumps,"." *Journal Hydraul Researcher IAHR* 29 (2): 207–218. doi:10.1080/00221689109499004.

MacDonald, R. G., J. Alexander, J. C. Bacon, and M. J. Cooker. 2009. ""Flow Patterns, Sedimentation and Deposit Architecture under a Hydraulic Jump on a Non-Eroding Bed: Defining Hydraulic-Jump Unit Bars,"." *Sedimentology* 56 (5): 1346–1367. doi:10.1111/j.1365-3091.2008.01037.x.

Murzyn, F., and H. Chanson. 2009. ""Free-Surface Fluctuations in Hydraulic Jumps: Experimental Observations,"." *Experiments Thermal Fluid Sciences* 33 (7): 1055–1064. doi:10.1016/j.expthermflusci.2009.06.003.

Novák, P., and J. Cabelka. 1981. *Models in Hydraulic Engineering; Physical Principles and Design Applications*, 459. London, UK: Pitman Advanced Publishing Program.

Parker, G. 1996. ""Some Speculations on the Relation between Channel Morphology and Channel-Scale Flow Structures,"." In *Coherent Flow Structures in Open Channels*, edited by P. J. Ashworth, S. J. Bennett, J. L. Best, and S. J. McLelland, 423–459. Chichester: Wiley.

Parker, G., and N. Izumi. 2000. ""Purely Erosional Cyclic and Solitary Steps Created by Flow over a Cohesive Bed,"." *Journal Fluid Mechanisms* 419: 203–238. doi:10.1017/S0022112000001403.

Piquet, J. 1999. *Turbulent Flows: Models and Physics*, 761. Berlin, Germany: Springer.

Ponsy, J., and M. Carbonnell. 1966. "Etude Photogrammétrique d'Intumescences Dans Le Canal De l'Usine d'oraison (Basses-Alpes)," ("Photogrammetric Study of Positive Surges in the Oraison Powerplant Canal,")." *Journal Social Française De Photogram (In French)* 22: 18–28.

Reungoat, D., H. Chanson, and C. E. Keevil. 2015. ""Field Measurements of Unsteady Turbulence in a Tidal Bore: The Garonne River in October 2013,"." *Journal Hydraul Researcher IAHR* 53 (3): 291–301. doi:10.1080/00221686.2015.1021717.

Reungoat, D., X. Leng, and H. Chanson. 2017. ""Successive Impact of Tidal Bores on Sedimentary Processes: Arcins Channel, Garonne River,"." *Estuar Coast Shelf Sciences* 188: 163–173. doi:10.1016/j.ecss.2017.02.025.

Schlichting, H., and K. Gersten. 2017. *Boundary-Layer Theory*, 805. 9th Edition ed. Berlin, Heidelberg: Springer-Verlag.

Shuto, N. 1985. ""The Nihonkai-Chubu Earthquake Tsunami on the North Akita Coast,"." *Coast Engineering Japanese* 28: 255–264. doi:10.1080/05785634.1985.11924420.

Tanaka, N., J. Yagisawa, and S. Yasuda. 2012. ""Characteristics of Damage Due to Tsunami Propagation in River Channels and Overflow of Their Embankments in Great East Japan Earthquake,"." *International Journal of River Basin Management* 10 (3): 269–279. doi:10.1080/15715124.2012.694365.

Treske, A. 1994. ""Undular Bores (Favre-Waves) in Open Channels - Experimental Studies,"." *Journal Hydraul Researcher IAHR* 32 (3): 355–370. Discussion **33**(2), 274–278, 10.1080/00221689509498675. doi: 10.1080/00221689409498738.

Tricker, R. A. R. 1965. *Bores, Breakers, Waves and Wakes*, 250. New York, USA: American Elsevier.

Viollet, P. L., J. P. Chabard, P. Esposito, and D. Laurence. 2002. *Mécanique des Fluides Appliquée. Ecoulements Incompressibles dans les Circuits, Canaux et Rivières, autour des Structures et dans l'Environnement*. 2ème édition, Paris, France: Presses des Ponts et Chaussées. 367. (in French).

Wang, H. [2014] "Turbulence and Air Entrainment in Hydraulic Jumps," *Ph.D. thesis* School of Civil Engineering, The University of Queensland, Brisbane, Australia, 341 pp & Digital appendices, doi: 10.14264/uql.2014.542.

Wolanski, E., D. Williams, S. Spagnol, and H. Chanson. 2004. ""Undular Tidal Bore Dynamics in the Daly Estuary, Northern Australia,"." *Estuar Coast Shelf Sciences* 60 (4): 629–636. doi:10.1016/j.ecss.2004.03.001.

Yasuda, H. 2010. ""One-Dimensional Study on Propagation of Tsunami Wave in River Channels,"." *Journal Hydraul Engineering ASCE* 136 (2): 93–105. doi:10.1061/(ASCE)HY.1943-7900.0000150.

Yeow, S. C., H. Chanson, and H. Wang. 2016. "Impact of a Large Cylindrical Roughness on Tidal Bore Propagation." *Canada Journal Civil Engineering* 43 (8): 724–734. doi:10.1139/cjce-2015-0557.